Thermoelectric Power Production Efficiency Can Surpass Photovoltaics Under Concentrated Sunlight Due to High-Temperature Performance Degradation

Matthew J. Traum & Juliana Mishur

Mechanical and Aerospace Engineering Department, University of Florida, Gainesville, FL 32611, USA

Abstract— **As of 2019, almost 97% of utility-scale solar power capacity is photovoltaic-based. Photovoltaic cells become less efficient at higher temperatures, requiring cooling water for these plants to maintain efficiency. However solar plants are often located in deserts where water is scarce, thus increasing the price of concentrated solar power. An unutilized but attractive alternative is thermoelectric generators under concentrated sunlight with passive geothermal cooling. This paper calculates the crossover temperature at which thermoelectric generator efficiency exceeds photovoltaic cell efficiency due to rising thermoelectric efficiency as operating temperature increases. The crossover temperature was determined to be 495K by theoretical modeling. A comparison of empirical literature for thermoelectric generators and experimental results for photovoltaic cells was conducted. To experimentally represent thermoelectric generators, metal collector targets were placed under two different Fresnel lenses with lens-to-collector target ratios of 28.8:1.0 and 275.0:1.0. Thermoelectric generators should always be considered as an alternative to a photovoltaics in concentrated solar power plants without coolant when the lens-to-target area ratio exceeds 350. For thermoelectric generators, heat flux absorption and corresponding elevated power generation are hindered by sunlight reflection. To improve heat flux absorption, the experimental setup was modified to include black acrylic or refractory painted collector targets. These treatments decreased reflectivity from 93 ± 2% for polished brass to 79 ± 2% and 92 ± 1% for 28.8:1.0 and 275.0:1.0 area ratio, respectively. With dramatic surface reflectivity reduction, thermoelectric generators will outperform photovoltaic cells as an alternative solar concentrating power plant when cogeneration is unneeded.**

Index Terms—thermoelectric generator, concentrated solar power, reflectance, photovoltaic cell

Nomenclature and Subscripts—

A_{lens}	=	area of solar concentrator, [m²]
A_{target}	=	area of a collector target, [m²]
A_{TE}	=	area of solar generator, [m²]
c	=	specific heat of the target material, [J/kg-K]
$\dot{E}_{sun}$	=	solar energy flux density, [W/m²]
h	=	average forced convection coefficient, [W/m²-K]
k_{TE}	=	thermal conductivity of TEG, [W/m-K]
L_{TE}	=	thermoelectric characteristic length of TEG, [m]
m	=	mass of the target material, [kg]

t	=	time, [s]
T_{high}	=	high temperature, [K]
T_{PV}	=	PV generator temperature, [K]
$T_{PV, ref}$	=	reference temperature of PV, [K]
T_{TE}	=	temperature of TEG, [K]
$T_{TE,cold}$	=	TEG cold end temperature, [K]
$T_{TE,hot}$	=	TEG hot end temperature, [K]
T_∞	=	ambient temperature, [K]
$T_{PV, ref}$	=	reference temperature of PV, [K]
z	=	thermoelectric figure of merit, [1/K]
α	=	coefficient of PV efficiency degradation with increased temperature, [-]
β	=	reference cell temperature coefficient, [%/K]
η_{PV}	=	temperature-dependent energy conversion efficiency of a PV generator, [%]
$\eta_{TE}[T_{TE,hot}]$	=	temperature-dependent energy conversion efficiency of a TEG, [%]
ρ	=	surface reflectivity, [-]

I. INTRODUCTION

As of 2019, about 97% of utility-scale solar power capacity is photovoltaic cell-based [1]. Although studies exist suggesting possible performance improvements [2], photovoltaic (PV) cells are nonetheless inefficient electrical power generators at higher operating temperatures. Utility-scale solar power plants often require active water cooling to maintain efficiency. Since many utility-scale solar power plants are situated in deserts where water is scarce, the use of water for cooling has raised concerns among environmentalists. For example, two 268 MW wet-cooled concentrated solar power (CSP) plants planned for Nevada's Amargosa Valley were projected to use 3,000 acre-feet (0.978 billion gallons) of water annually, which is enough to provide for 3,125 typical American homes [3]. In part due to water use issues, this plan was never implemented. Instead, a much smaller 100 MW conventional photovoltaic plant was built [4]. The costs of mitigating water usage increase the price of CSP in desert regions, reducing its economic viability.

Numerous studies exist suggesting a variety of methods to combine thermoelectric generators (TEG) with PV cells in

hybrid power plants to harvest excess waste heat for additional energy generation and provide PV cooling. A recent review is given by Narducci & Lorenzi [5]. Specific schemes include spectrum splitting [6], two-stage TEG thermal harvesting [7], and thermally bridging the PV and TEG with conductive paste [8]. Each of these techniques is predicated on the TEG facilitating heat transfer from the PV to improve efficiency.

Instead of working against high CSP PV lens temperature with a backing TEG, water flow, or other cooling system, an alternative is explored in this study: eliminate the PV, concentrate sunlight directly on the TEG, and provide a heat sink with passive geothermal cooling. This study shows that even at modest concentration ratios, TEG exceeds PV as the preferred solid state energy conversion technology owing to the increasing TEG efficiency as its operating temperature increases.

II. LITERATURE REVIEW

An overwhelming volume of research on large-scale CSP energy generation exists [9, 10] including Fresnel lenses for large-scale PV systems [11, 12]. The literature reveals two CSP production efficiency limitations: 1) PV efficiency decreases with increasing temperature, and 2) there exists a PV saturation limit where no additional electrons are produced despite increased photon flux. The concentration of sunlight on the PV exacerbates both these limitations.

In contrast, TEGs are solid-state heat engines. Their efficiency increases as the hot reservoir temperature increases, and power generation is constrained only by the component melting temperature [13, 14].

Xia et al. reviewed state-of-the-art TEGs [15]. Similar to conventional heat engines, TEGs operate across temperature gradients [16, 17]. When the junctions of dissimilar materials are maintained at different temperatures, a proportional voltage is generated. Conventional solar TEGs capture sunlight without concentration. A successful demonstration of this approach is the concept of a thermoelectric roof solar lens (TE-RSC) by Maneewan et al. [17]. TE-RSC is a residential-roof-integrated system meant for hot and humid environments in which TEGs collect sunlight to power fans within the building's attic. Air circulation simultaneously provides convective cooling to the home while rejecting entropy from roof-integrated TEGs. In tests at 1000 W/m² solar flux and representative environmental conditions, a TE-RSC simulator achieved 4.24% energy conversion efficiency with a hot side temperature of 345.8 K and cold side temperature of 319.2 K. The corresponding ceiling heat transfer rate reduction was about 3–5 W/m², and the estimated annual electrical energy savings was ~362 kW-h, corresponding to a simple payback period of 4.36 years [18]. Critically, this system required no water coolant to function.

Hybrid solar PV/TEG systems synthesize both solid-state energy converters to recover low-grade thermal energy excess solar energy at wavelengths not captured by PV. For example, Kraemer et al. [19] proposed partitioning the solar spectrum into wavelengths matched to photovoltaic bandgaps and using the remaining spectrum to heat TEGs. However, this approach achieved only marginal efficiency gains. Vorobiev et al. [20]

postulated a new PV material that is transparent to non-absorbed solar wavelengths. This material passes light and cannot be absorbed by a TEG. The proposed preferentially transparent PV material was not reduced to practice. Alamri et al. [21] upcycled a satellite dish by silvering it for CSP and then backed the PV with TEG at the dish's focal point for bottoming thermal energy capture. This scheme worked at the small scale of a few watts, but it proved difficult to scale up.

CSP TEGs produce remarkably high focal point temperatures on the TEG hot side [22]. As shown later, TEGs exhibit a heat-engine-like property of increasing thermodynamic efficiency as the hot/cold temperature gradient across them increases. Moreover, TEGs are costly, but concentrator lenses and mirrors are inexpensive. Large-area energy capture concentrated on a small focal point reduces required TEG size and cost.

Rockendorf et al. [23] published a pejorative CSP TEG versus CSP PV comparison, which warrants reexamination. They concluded that the CSP PV is superior to the CSP TEG in solar-to-electrical energy conversion efficiency and total efficiency when waste heat recovery is considered. However, tests producing these conclusions were conducted in regimes that favored and promoted PV performance while disadvantaging the TEG. A separate solar concentrator collected heat from the TEG hot side and transferred it via the working fluid to a separate active water loop that cooled the PV system to its ideal operating temperature. Heat exchangers provided thermal interaction between this hot working fluid and the TEG hot side, as well as between the TEG cold side and a cooling loop for combined heat and power. According to Rockendorf et al., the necessary operating TEG hot-side temperature prevented the working fluid from absorbing solar thermal power from the concentrator.

Other TEG experts have suggested that TEG's show CSP energy generation promise, but with the expectation of studies involving exotic thermionic/thermoelectric conversion systems [24], practical applications are sparse [25].

This present study sets theoretical foundations for both TEG and PV performance efficiencies. It then evaluates the empirical literature results for the proposed TEG apparatus and compares them with the experimental results for the PV. Finally, this study outlines the major findings and economic analysis, justifying the use of TEG as a PV alternative. Fig. 1 captures the methodology flowchart to improve the comprehension of how the work was carried out in Sections III through VI.

III. PROPOSED APPARATUS

Fig. 2 shows the CSP TEG apparatus evaluated in this study. TEGs connected to a deep-ground thermal sink do not consume any water and can operate at elevated temperatures for extended periods with no moving parts. The anticipated TEG maintenance-free lifetimes exceed 100,000 hours (11.4 years) [22, 24, 26]. The generator would be mounted on a metal pole sunk at least 12 m into the ground to reach below the thermal inversion depth [27]. The deep ground serves as a constant-temperature heat sink for the TEG cold end. The TEG hot end

sits at the focus of a sun-tracking solar concentrator, which can be a Fresnel lens, parabolic dish, trough, or another combination of optics that keep sunlight focused on the TEG throughout the day.
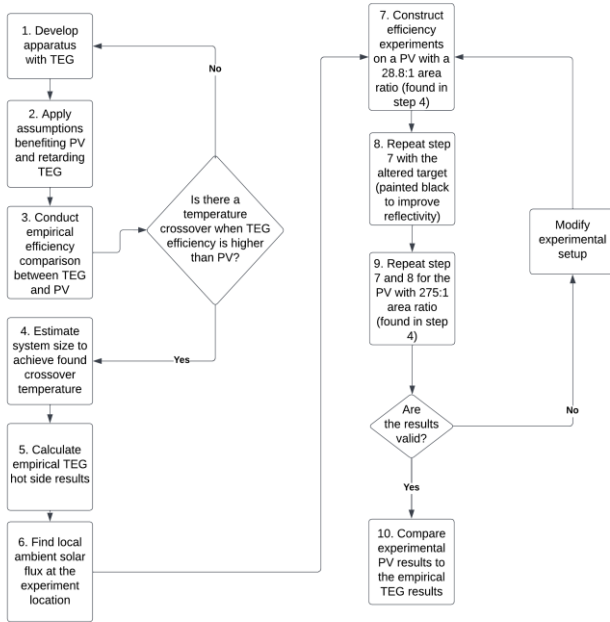
occur if a well-designed thermal collector target with Biot < 0.1 is used. Thus, CSP optics must only be sophisticated enough to ensure that the focus strikes somewhere on the collection surface target throughout the day.

IV. THEORETICAL MODELLING

Theoretical analysis aimed to answer two questions:1) is there a temperature crossover where $\eta_{TE} > \eta_{PV}$ below the TEG melting point, and 2) is the crossover temperature achievable at a realistic solar concentration ratio.

A. Efficiency Comparison for TEG and PV Generators

To provide a theoretical comparison between PV and TEG under concentrated sunlight, performance models were developed for each configuration, with assumptions intentionally yielding the best case for PV and the worst case for TEG. A strong case to pursue CSP TEGs exists if the TEG proves superior under assumptions favorable to PV.

The temperature-dependent energy conversion efficiency of a TEG (1) [29] is contingent upon three parameters:1) hot-end temperature, 2) cold-end temperature, and 3) thermoelectric figure of merit.

Fig. 1. *Methodology flowchart used in this study.*

$$\eta_{TE}[T_{TE,hot}] = \frac{(T_{TE,hot} - T_{TE,cold})}{T_{TE,hot}} \frac{\sqrt{1 + z\left(\frac{T_{TE,hot} + T_{TE,cold}}{2}\right)} - 1}{\sqrt{1 + z\left(\frac{T_{TE,hot} + T_{TE,cold}}{2}\right)} + \frac{T_{TE,cold}}{T_{TE,hot}}} \quad (1)$$

The assumption that the TEG cold end is in perfect thermal communication with an infinite cold reservoir at $T_{TE,cold} = 300$ K (approximately ambient temperature), was applied to (1). The thermoelectric coefficient was approximated as z = 0.0013 1/K, which is an empirical value for Bi_2Te_3 thermoelectric material under an 88.1 K temperature gradient at a mean temperature of 322 K (reported cold side ~ 290 K and hot side ~ 378 K) [26]. A z value lower than that conventionally reported for thermoelectric materials was chosen because of the large temperature gradient, as some degradation in z under this condition has been observed [26].

While it was further assumed for this analysis that z is not a function of temperature, Muto et al. [27] reported the Bi_2Te_3 temperature dependence of z for a TEG hot side temperature up to ~ 471 K under ΔT ~ 160 K. For these specific test conditions, the smallest reported intrinsic (i.e., device-independent) z was approximately 0.003 1/K. For experimental thermoelectric materials specifically designed to function at high temperatures under concentrated sunlight, the device figure of merit (zT) has been shown to remain constant from room temperature to 600 K [30]. That is, z ∝ 1/T for these materials in this temperature range. The use of the approximation z = 0.0013 1/K (independent of temperature) is therefore justified because this value is a likely lower bound on the actual property value that would be encountered in the real system for the range of temperatures encountered.

Fig. 2. *Planned solar concentrating thermoelectric generator schematic.*

Because TEGs absorb thermal energy rather than light, the collected sunlight need not be focused directly on the hot side of the TEG. Instead, a thermally conductive heat lens/spreader with surface area exceeding that of the TEG hot side can pass heat by conduction to the hot end. Lashin et al. [28] model performance of a partially illuminated CSP TEG, but the TEG hot end temperature gradients suggested by that work will not

Certainly, more sophisticated models exist to approximate TEG performance at variable temperatures [31]. However, the

simplified analysis here is adequate to conclude that TEG outperforms PV on an efficiency basis at elevated temperatures, while allowing prediction of the temperature at which efficiency crossover occurs.

The coefficient of efficiency degradation with increasing temperature for silicon PV is between -0.003%/K and -0.006%/K from a reference temperature of 300K [32]. To provide the most favorable case for PV efficiency, β = -0.003%/K was selected and was not considered a function of temperature. Field deployed flat plate single crystalline silicon PV modules have a maximum measured efficiency not exceeding 12% (at $T_{PV,ref}$ = 300 K) [33, 34]. The reference cell temperature coefficient for silicon PV is between -0.003%/K and -0.006%/K (at $T_{PV,ref}$ = 300 K) [32, 35, 36]

Because the intent of this analysis is to examine conditions where TEG performance exceeds PV performance, the parameters in the PV model (2) are selected to provide an upper bound on the PV performance. At temperatures where the lower-bound TEG model exceeds the performance of the upper-bound PV model, we are assured that the TEG will outperform the PV. Thus, to provide the most favorable case for PV efficiency, it is assumed that α = 0.12 and β = -0.003%/K, and that these parameters are not functions of temperature. The experimental evidence detailed below demonstrates that these parameter selections are wildly optimistic in comparison to the real PV cell performance. Combining these empirical parameters into an equation for PV efficiency as a function of temperature yields.

$$\eta_{PV}[T_{PV}] = \beta\{1 + \alpha(T_{PV} - T_{PV,ref})\} \qquad (2)$$

The linear relationship between the PV cell temperature and efficiency was experimentally verified for concentrated PV by Kemmoku et al. [36].

To provide a technically fair comparison between TEG and PV, neither (1) nor (2) was modified to include the impact of external solar concentration. These equations predict the efficiency, that is, the ratio of power output to input, where the input power is taken just above the TEG or PV lens surface with no concentrating optics involved. This control surface is shown in Fig. 3. In the forthcoming analyses, this approach is justified for two reasons. First, all else being equal, concentrating optics on the TEG provides the same net energy density concentration as the identical optics for the PV. Therefore, any net efficiency improvements cancel each other when compared. Second, while PV is sensitive to the incident light angle, TEG is not. To contain costs, CSP systems employ lenses that concentrate sunlight but not condensers to reorient collected light to arrive perpendicular to the flat PV cell surface. Concentrating optics thus have disproportionate positive benefit for TEG over the PV. Rather than directly comparing the efficiencies of PV and TEG lenses, this study includes bounding assumptions that benefit PV while hindering TEG efficiency. Thus, not including the impacts of external solar concentration on the efficiency of both system types was an intentional choice, consistent with the bounding assumption approach of this study.

As shown later, the models of (1) and (2) predict the conditions under which the TEG performance exceeds the PV

performance. As temperature increases above ambient, TEG efficiency improves from 0%, while PV efficiency decreases from 12%. Near a temperature of 495 K, these two curves cross at approximately 5% efficiency. Additional temperature increases further improve the TEG efficiency while degrading that of PV. Thus, the target TEG hot-side temperature above 495 K was established as a design parameter for the proposed system.

B. Energy Balance for Solar Generators under Concentrated Sunlight

To estimate the system size that achieves a 495 K efficiency crossover temperature, the ratio of the solar concentrator to solar generator area is needed. The first law of thermodynamics applied to a control volume containing a TEG is schematically shown in Fig. 3. The following modeling assumptions were applied:1) the system cannot store energy and is operating at steady state; 2) unless otherwise noted, variables are not functions of temperature; 3) the spatial temperature across the hot side of the system is uniform; 4) all sunlight that strikes the concentrating lens is focused onto the TEG; 5) the ambient temperature and the temperature on the TEG cold side are fixed at 300 K; 6) the system has a uniform reflectivity on its exposed top surface; 7) the exposed face of the target exchanges heat only via forced convection with air blowing over this surface and radiation to the ambient; and 8) once absorbed, no heat is lost from the target except via convection/radiation from the top and conduction through the bottom.

In this model, the average forced convection coefficient, h = 21.7 W/m²-K, was obtained from a correlation for laminar flow over a 10 cm long flat plate [37] under a constant air velocity of 3 m/s. The surface's solar reflectivity was estimated to be 0.738 for emery-paper-polished brass [38] and 0.06 for low-reflectivity black paint [39].
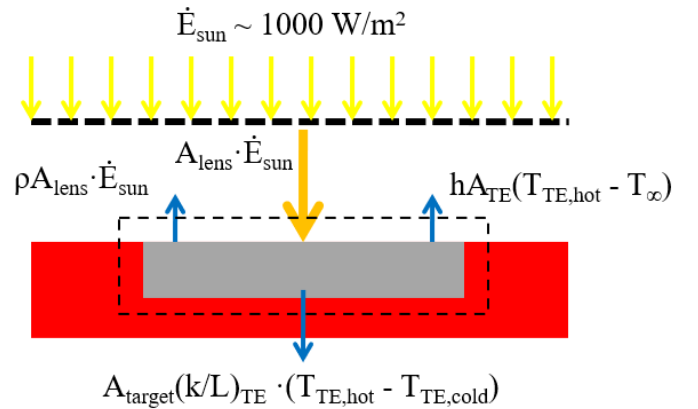

$\dot{E}_{sun} \sim 1000$ W/m²

$\rho A_{lens} \cdot \dot{E}_{sun}$ $A_{lens} \cdot \dot{E}_{sun}$ $hA_{TE}(T_{TE,hot} - T_{\infty})$

$A_{target}(k/L)_{TE} \cdot (T_{TE,hot} - T_{TE,cold})$

Fig. 3. *An energy flow accounting model for a TEG under concentrated sunlight.*

The resulting equation is

$$0 = A_{lens}\dot{E}_{sun} - \rho A_{lens}\dot{E}_{sun} - hA_{target}(T_{TE,hot} - T_{\infty})$$
$$- A_{target}\left(\frac{k_{TE}}{L_{TE}}\right)(T_{TE,hot} - T_{TE,cold}) \qquad (3)$$

The first term is the energy focused on the target, the second term is the incident energy reflected away from the target, the

third term is the energy convected and radiated away from the top of the target, and the final term is the energy conducted from the target to the hot side of the TEG material. The final term depends on the TEG material and physical parameters. $k_{TE} = 2.4$ W/m-K was selected for modeling, which is the highest value given for Bi_2Te_3 at elevated temperatures by Muto et al. [27]; $L_{TE} = 0.007$ m, a typical TEG energy converter thickness, was also selected. Rearranging (3) to solve for A_{lens}/A_{target} and noting that $T_{TE,cold} = T_\infty$ yields (4).

$$\frac{A_{lens}}{A_{target}} = \frac{\left(h + \left(\frac{k_{TE}}{L_{TE}}\right)\right)\left(T_{TE,hot} - T_\infty\right)}{\dot{E}_{sun}(1 - \rho)} \qquad (4)$$

By eliminating paths of thermal energy leakage that might be present and appreciable in the real system, the above simplifying assumptions, especially (8), yield a lower bound on the ratio A_{lens}/A_{target} required to achieve $T_{TE,hot} = 495$ K. Inserting numbers into (4) at the 495 K efficiency crossover point gives for $A_{lens}/A_{target} = 271.3$ for a polished brass target and 75.6 for a black painted target. Because the experimental system described here only consists of a hot-side target material enclosed within insulating fireclay bricks (except for the top), the experiments provide negligible conductive paths to a cold temperature reservoir. Removing this term from (4) yields

$$\left(\frac{A_{lens}}{A_{target}}\right)_{insulated} = \frac{h\left(T_{TE,hot} - T_\infty\right)}{\dot{E}_{sun}(1 - \rho)} \qquad (5)$$

TABLE I
PARAMETER VALUES APPLIED TO SOLUTION OF (4) AND (5)

Parameter	Units	Value
$T_{TE,hot}$	[K]	495
$T_{TE,cold}$	[K]	300
T_∞	[K]	300
Z	[1/K]	0.0013
H	[W/m²-K]	21.7
$\dot{E}_{sun}$	[W/m²]	1000
ρ	[-]	0.05
k_{TE}	[W/m-K]	2.4
L_{TE}	[m]	0.007

Inserting numbers into (5) at the 495 K efficiency crossover point gives $A_{lens}/A_{target} = 16.2$ for a polished brass target and 4.5 for a black-painted target surface. Table 1 lists the parameters used in (4) and (5) to provide reasonable initial A_{lens}/A_{target} design guidance as the area ratio threshold for concentrating solar energy systems, beyond which TEG should be considered in place of PV. Given this analytical guidance, two experimental apparatuses were designed and built, and their thermal performances were expected to closely match the assumptions and parameters underlying (4) and (5) to validate the modeling approach. The first experiment had an A_{lens}/A_{target} ratio of 28.8:1.0, approximately matching the 16.2:1.0 result of (5) for a polished bass target. The second experiment had an A_{lens}/A_{target} ratio of 275.0:1.0, closely matching the 271.3:1.0 result of (4) for a polished brass target.

C. Transient and Steady Thermal Behavior of Hot Side Target Under Concentrated Sunlight

The thermal response of the system under concentrated sunlight is modeled using a lumped mass control volume containing only the brass target material and subjected to the following assumptions:1) the material does not change phase; 2) its specific heat is not a function of temperature; 3) the control volume is thermally insulated on all external surfaces, except the upward-facing surface, with a perfect adiabatic boundary; 4) the upper surface of the target receives a spatially uniform flux of solar energy, and a portion of this energy is absorbed while a part is reflected; 5) the reflectivity of the exposed surface is completely uniform and not a function of temperature; 6) the upper surface also experiences forced convective heat transfer to a stream of air arriving at ambient temperature and radiation heat transfer to the environment at ambient temperature; and 7) regardless of the system temperature, natural convection is negligible compared to forced convection and radiation and is ignored. Under these assumptions, the first law of thermodynamics applied to this lumped-parameter model yields the following expression:

$$(1 - \rho)\dot{E}_{sun}A_{lens} = hA_{TE}(T_{TE} - T_\infty) + mc\frac{\partial T_{TE}}{\partial t} \qquad (6)$$

The different operating conditions applied to (6) enables the measurement of important experimental parameters. In the early period of the warm-up transient from ambient temperature, the convective heat transfer term is negligible provided that $T_{TE} \sim T_\infty$, as shown in (6) becomes.

$$(1 - \rho)\dot{E}_{sun}A_{lens} = mc\frac{\partial T_{TE}}{\partial t} \qquad (7)$$

If the mass and specific heat of the target material are known, then the measured temperature change with time provides the energy absorbed by the target material. The experiment effectively becomes a pyranometer for measuring its own absorbed solar energy. Moreover, if the total solar energy flux is measured independently, (6) can be solved for the solar spectrum reflectivity of the target material.

Returning to (6), when steady-state conditions are achieved at elevated temperatures, the temperature derivative with respect to time vanishes to zero: $\partial T_{TE}/\partial t \rightarrow 0$. Under these conditions, (6) becomes.

$$(1 - \rho)\dot{E}_{sun}A_{lens} = hA(T_{TE} - T_\infty) \qquad (8)$$

The absorbed solar energy, determined from the experimental measurements and (6) is known. The ambient temperature and target material temperature are also known empirically. Thus, (8) can be solved for the forced convection coefficient: Finally, when sunlight strikes and the target is blocked, solar energy is no longer absorbed by the target material. (6) can be rewritten and integrated into the following

form,

$$T_{TE}(t) = (T_{high} - T_\infty)e^{-\frac{hA_{lens}}{mc}t} + T_\infty \qquad (9)$$

This classic Newtonian cool-down expression independently verifies the experimentally measured forced convection/radiation coefficient obtained using (8). The addition of a pyranometer in the plane of the solar collection aperture and an anemometer placed downstream of the target material to measure the airflow over its upper surface enables further validation and verification of the thermal behavior of the target material by comparison with (7), (8), and (9). These equations also enable the analysis and evaluation of the performance of the experimental system for comparison with the idealized analytical model described by (4).

V. EXPERIMENTAL METHODS

Six independent experiments and tests were performed to gather relevant local solar flux data, confirm the mechanisms for PV performance degradation under concentrated sunlight, and evaluate the thermal performance of the brass TEG hot-side targets.

A. Local Ambient Solar Flux

All data were obtained from the south-facing courtyard of the Discovery Park facility at the University of North Texas, located at 3940 N Elm St, Denton, TX, USA 76207. Some data presented in the Results section were obtained before a pyranometer was available for instantaneous solar flux monitoring. For these early experiments, the collection aperture was oriented normal to the sun, and a solar flux of 1000 W/m² was assumed because instantaneous solar flux data for Denton, TX (where the experiments were conducted) were not available. To confirm the validity of this assumption for a typical cloudless Denton spring day, an Apogee SP-110 pyranometer was placed sighting straight up on a residential rooftop above tree and building levels to eliminate shadowing. Pyranometer output was logged at 2 Hz using the voltmeter setting of an Extech 380900 multimeter. The resulting horizontal flat plate solar flux curve for a full day, shown in Fig. 4, confirms the validity of the 1000 W/m² solar flux assumed in the early experiments; this datum appears at the peak of the recorded data.

B. PV Maximum Power Point Determination

The PV output power shifts as the cell temperature fluctuates and as the load across the PV array changes. Large PV installations use automatic maximum power point (MPP) tracking to adjust the direct current load resistance across their arrays as the conditions change to maximize the power derived from the PV. MPP trackers consume power parasitically, but this loss is more than offset by the extra power production enabled by large PV arrays using MPP tracking.
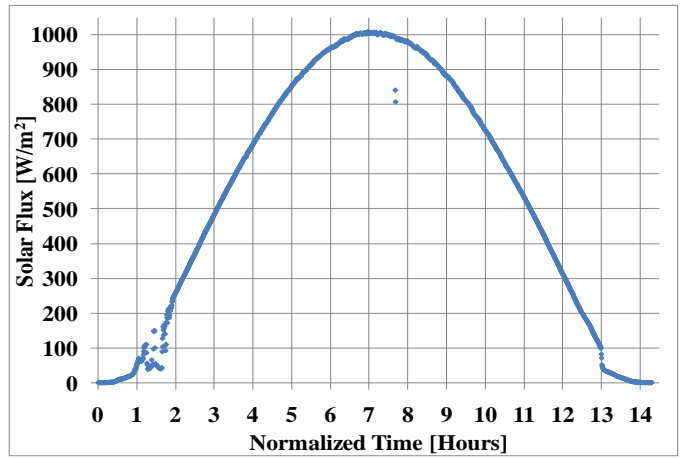

Fig. 4. Instantaneous solar flux on a near-cloudless day in Denton, TX, USA taken on April 22, 2009.

To experimentally evaluate the temperature degradation of the PV efficiency, the direct-current resistive load yielding the MPP for each PV panel was identified at 300 K and used for all subsequent experiments. We concede that the MPP load at room temperature for a PV cell may not correspond to its MPP load at elevated temperatures. Nonetheless MPP resistance evaluated at room temperature was used as a representative value.

To find the MPP for a representative PV cell, a Radio Shack 25 Ω three-terminal rheostat was wired across the leads of the PV cell to provide a variable load. Using a PASCO Data Studio PASPORT power sensor, the ammeter function was wired in series to measure the current through the rheostat, whereas the voltmeter function was wired in parallel to measure the voltage across it. The rheostat central lead and its unused terminal were attached to a Cen-Tech pocket digital multimeter in resistance meter mode. Before the experiment, the total rheostat resistance was measured to be 25.1 ± 0.1 Ω. This wiring arrangement enabled determination of the resistance applied to the PV cell by subtracting from 25.1 ± 0.1 Ω the resistance meter reading.
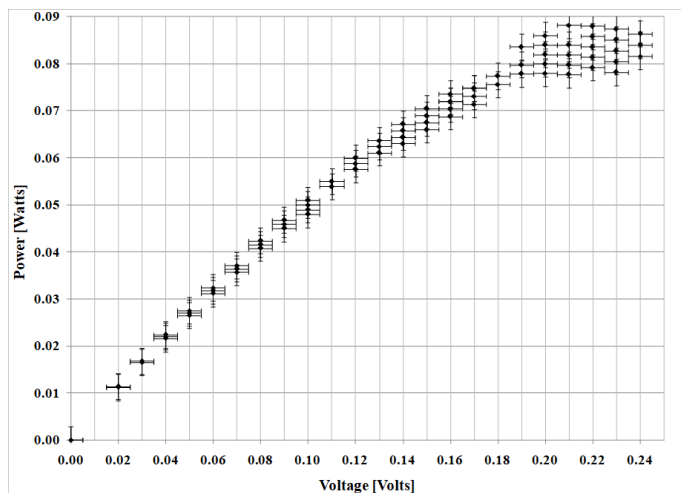

Fig. 5. Experimental PV cell power-voltage curve shows the MPP at 0.22 volts and 0.42 amps, which corresponds to a load of 2.5Ω.

A Solar World 4-600 solar cell (the type used for temperature-efficiency degradation tests, below) was removed from its encapsulation module and set at 70 ± 0.5 cm) from a Newport 67005 sun lamp with an Oriel 62020 light filter (1.5 Air Mass Coefficient [AMC]), which was powered by a Newport 69911 power supply set at 160 watts for this experiment. With the PASCO Data Studio logging voltage across and current through the rheostat, the rheostat resistance was slowly decreased across the full range. The resulting power-voltage data for the PV cell are given in Fig. 5, and the MPP corresponds to a rheostat setting of 2.5 Ω, which gave 0.22 volts at 0.41 amps: 0.09 watts.

C. PV Efficiency Degradation at Elevated Temperature

To measure the PV efficiency degradation at elevated temperatures for comparison with (2), a Solar World 4-600 PV cell (removed from its encapsulation module) was affixed to a Provocraft Candlscense candle warmer using a temperature resistant RTV adhesive. The AC power to the candle warmer was controlled with a Proformax SRV-10 Variac transformer, whose voltage output was monitored using an Extech MultiMasterTM 570 true RMS multimeter. The temperature of the PV cell was adjusted by varying the Variac power output of the candle warmer.

As shown in Fig. 6, the PV heater assembly was arranged to hang vertically and was placed 38 ± 0.5 ~ cm from the Newport 67005 sun lamp with an Oriel 62020 filter lens (1.5 AMC) and a Newport 69911 power supply. The sun lamp power supply was set to an output of 160 Watts throughout the experiment, corresponding to a solar flux of 960 ± 10 w/m^2. The solar flux was never changed in this experiment to ensure that the efficiency degradation with temperature was isolated from the degradation related to photon saturation.

The solar flux was determined after the experiment by placing an Apogee SP-110 pyranometer at the same distance from the sun lamp as the PV cell and measuring the output with an Extech 380900 logging multimeter.

During the experiment, the instantaneous temperature of the PV cell was measured using a single Omega Engineering 5SC-TT-K-40-36 K-type thermocouple affixed to the center of the cell on the exterior face with a high-temperature-resistant electrical tape. The fixture point and thermocouple wire path running away from the assembly were co-located along a PV cell metal pick-up such that no light incident on the active lens surface was blocked. The thermocouple was monitored using an Omega OM-2041 portable data logger, and the PV cell voltage and current output were monitored using an Extech 380900 logging multimeter. A rheostat set to 2.5 Ω (the room-temperature MPP load, determined previously) was wired across the PV cell to provide a constant electrical load, which was continuously measured using a Cen-Tech pocket digital multimeter in the resistance meter mode.

Fig. 6. *PV temperature test experimental setup.*

The experiment was initiated by shining the sun lamp directly on the PV cell (covering it completely with light), turning the heater to output 100.3 VAC, and allowing the PV cell to warm to 380.3 K. Under these conditions, the temperature was allowed to settle to steady state. The steady temperature was defined throughout this experiment as the condition in which the measured PV temperature remained within 1 K of the observed temperature for 360 s. After recording data at each steady-state set point, the heater voltage was nominally reduced by 10 VAC, and the system was allowed to settle to a new steady-state temperature.

The experiment was conducted in the cool-down direction from a high voltage of 100.3 VAC to a low voltage of 0.0 VAC. The experiment was repeated in the heat-up direction starting at 5.15 VAC and increasing in nominal increments of 10 VAC. Although two different temperature directions were used to determine whether there was any direction-dependent hysteresis in the measurement, no hysteresis effect was observed as verified by error analysis described later in the PV Efficiency Degradation at Elevated Temperature section of Results.

D. PV Efficiency Degradation at Elevated Photon Flux

In addition to efficiency degradation with increasing temperature, efficiency degradation can also occur if incident photon flux is higher than the PV cell can absorb. The phenomenon of PV saturation under concentrated sunlight was mentioned by Kemmoku et al. [36], but was not experimentally pursued in that study. If this threshold flux is reached, sunlight that would normally be converted to electricity is absorbed as heat. Owing to the saturation limit, the PV power output remained constant beyond the solar flux threshold, even when the flux intensity was increased. The fixed power output, despite the increased solar flux input, manifests as a decreased efficiency. Although not considered here analytically, PV photon saturation could appear in solar concentrators with sufficiently high lens collector to PV cell area ratios. Therefore, we experimentally measured its onset using the setup shown in Fig. 7.
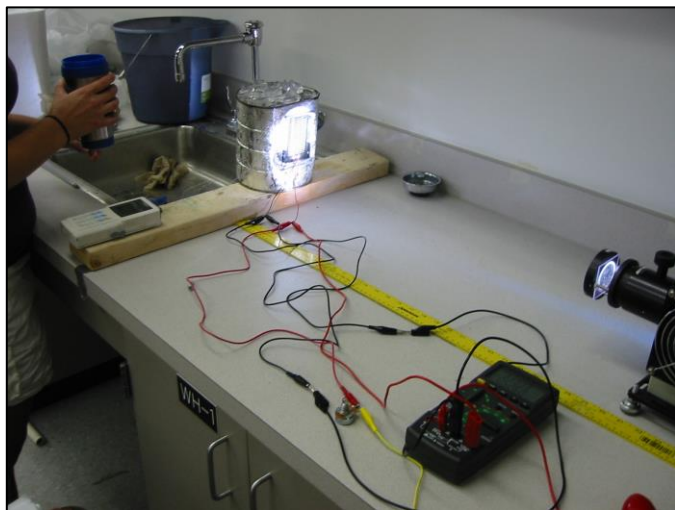
Fig. 7. PV photon saturation test experimental setup.

Fig. 8. Photon flux saturation data. PV output increases with available flux, plateaus at 1600 W/m², and then remains the same at higher flux rates indicating reduced energy conversion efficiency.

A Solar World 1.5-50 PV cell was removed from its protective casing and fixed to the face of a cubic metallic box with a high thermal conductivity epoxy. The PV cell voltage and current were logged using a custom National Instruments LabView instrument. A Radio Shack rheostat set to 50 Ω (the room-temperature MPP load for this type of PV cell) provided a constant electrical load, which was continuously measured via LabView.

The assembly was placed 50 cm away from a Newport 67005 sun lamp with an Oriel 62020 filter lens (1.5 AMC), using a Newport 69911 power supply. The sunlamp power supply was first set to 160 W, corresponding to a solar flux of 814 ± 10 W/m², which is below the PV photon saturation point, and the temperature was allowed to settle to a steady state. To collect data as a function of solar flux, the sun lamp power output was increased in increments of 10 watts up to 550 watts, which corresponds to a maximum solar flux of 2410 ± 10 W/m². The solar flux corresponding to each sun lamp power supply set point was determined after the experiment by placing an Apogee SP-110 pyranometer at the same distance from the sun lamp where the PV cell was located, and the output was measured with an Extech 380900 logging multimeter.

To ensure that the photon saturation experimental results were isolated from the PV efficiency degradation with increasing temperature, a single Omega Engineering TMQSS-020-12 T-type thermocouple was affixed to the center of the PV cell housing module on the duct-taped face abutting the cubic metallic box. The thermocouple was monitored using an Extech EA15 logging reader.

To maintain the PV cell temperature constant despite the increasing solar flux, the flattened metallic can to which the cell was affixed was filled with ice and water to serve as a cold thermostat. A pinhole made on the bottom of the can drain liquid water (and carry away thermal energy as latent heat). As the ice melted and drained, more ice and water were added to the can to maintain apparatus isothermal conditions. This control succeeded in maintaining the PV cell temperature between 288.5 K and 290.4 K throughout the test.
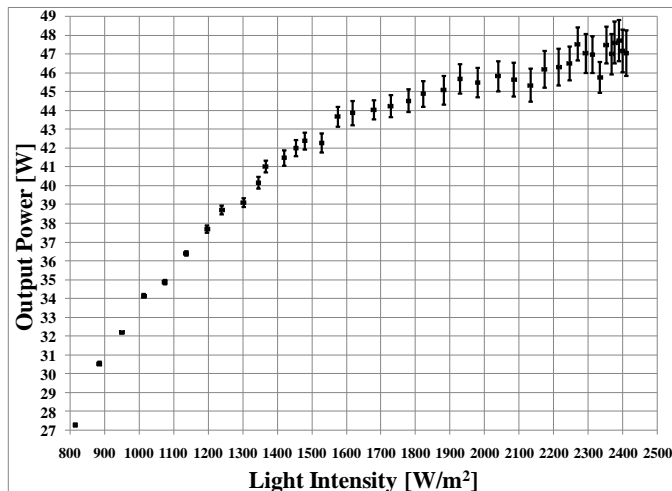
From temperature-related efficiency degradation data previously collected, a loss in total PV efficiency no greater than 0.015% was expected owing to the slight increase in temperature as solar flux was increased almost 3-fold. Therefore, this small effect is ignored. The results, given in Fig. 8, show a point of diminishing returns in PV power output for increasing solar flux at approximately 1600 W/m² and a complete leveling of PV power output at around 2000 W/m². Thus, for the cell tested, a concentrator aperture-to-PV cell area ratio of 2:1 would cause the onset of photon saturation.

E. Solar Collection Experiment at a 28.8:1.0 Concentration Ratio by Area

For these experiments, a square piece of Alloy 385 brass 5.46 ± 0.01 cm long by 5.46 ± 0.01 cm wide by 0.33 ± 0.01 cm thick and 77.311 ± 0.001 g in mass represented the TEG hot side concentrated sunlight collection target. In the first set of experiments, the brass surface was polished using 60-grit emery paper. In the second set of experiments, the polished surface was painted over with one coat of Golden Acrylics "Carbon Black" paint (Golden # 1040-4) to make the surface less reflective.

A single Omega Engineering 5SC-TT-K-40-36 thermocouple was soldered to the underside center of the brass square. This thermocouple type, made with 40 AWG wire, is the smallest commercially available readymade thermocouple and was chosen to minimize surface temperature measurement errors arising from the presence of the thermocouple on the brass as well as the thermocouple fin effect. Manufactured using "special limits or error" material, the thermocouple experimental error was ± 1.1 K. Temperature data were sampled at 1 Hz for the unpolished brass experiment and 0.0167 Hz for the black-painted brass experiment and recorded using an Omega Engineering OM-2041 portable data logger. The measurement error in the logger was ± 0.7 K for the temperature range of interest. Propagation of experimental error yields a measurement uncertainty no greater than ± 1.3 K. Using the highest experimentally measured forced convection heat transfer coefficient (h = 71 W/m²-K, described below), the Biot

number through the brass in the thickness direction was 0.002, whereas in the width direction, it was 0.035. Therefore, it is justified to assume spatial temperature uniformity across the brass, as measured by a fixed thermocouple.

The brass was mounted on an insulating fireclay brick support with a thermocouple facing downward (Fig. 9 and 10). A square crevice 0.33 cm deep was chiseled into the brick so that the brass square would lay flush with the brick's surface. The textbook thermal conductivity of fireclay brick is 0.72 W/m-K [40], and this specimen was at least 1.07 ± 0.01 cm thick in all directions surrounding the bass square. Neglecting the contact resistance (which provides additional thermal insulation, driving the real thermal conductance lower), the thermal conductance through the ceramic was at most 0.0077 W/K. The lowest experimentally measured thermal conductance due to forced convection and radiation over the brass plate was h = 27 W/m^2-K, described below, giving a thermal conductance of at least 0.081 W/K through this mechanism. Comparing the conductance of the brick insulator to forced convection and radiation, at most only 9.5% of the heat leakage from the brass square can be attributed to conduction through the brick, and this percentage is an upper bound. This result confirms that the brick approximates an adiabatic barrier to conductive heat transfer, as assumed in (3) and (6). Thus, in the models, all heat losses from the brass square target were assumed to arise from forced convection and radiation from the exposed surface.

Fig. 9. *Small-Area Fresnel solar concentrator apparatus with the brass target unpainted*

The air velocity, air temperature, and relative humidity over the brass square and the brick insulator were measured using a Kestrel 4000 pocket weather station with an anemometer fan 12 ± 1 cm from the leading edge of the brick support and 9 ± 1 cm from the leading edge of the brass square. Data collected by this instrument were recorded at 0.2 Hz, and the instrument's velocity, temperature, and relative humidity measurement uncertainties were ± 0.1 m/s, ± 1.0 K, and $\pm 3.0\%$ RH, respectively. Ambient temperature and relative humidity were measured using a CenterTek 313 logging hygrometer at a

sampling rate of 0.1 Hz. The experimental uncertainties in temperature and relative humidity were ± 0.7 °C, and $\pm 2.5\%$ RH, respectively. The logging hygrometer was placed at least 2 m from the experiment in the shade off the ground on a plastic-insulated bench to ensure accurate ambient readings beyond any interference from the experiment.

Fig. 10. *Small-Area Fresnel solar concentrator apparatus with the brass target painted black.*

The solar concentrating lens used in these experiments was a 29.3 ± 0.5 cm by 29.3 ± 0.5 cm square Fresnel lens scavenged from a 3M 910 Lamp Changer overhead projector. The aperture area of this lens was 858.5 ± 20.7 cm^2, 28.8 times larger than the area of the brass target. The lens was mounted on a pair of ring stands and situated over the brass square facing the sun, so the concentrated solar focal point targeted the center of the brass square (Fig. 9). The forced convection over the experiment was provided by a commercial off-the-shelf rotary fan with three qualitative settings: low, medium, and high. The face of the fan was situated coincident with the leading edge of the insulating ceramic brick, and the axis of the fan was offset from the brass square; thus, the edges of the blades were visually aligned with the edge of the brass square. This arrangement exposed the brass square to the fan wake near the edge of the blades, where the resulting air velocity was the highest.

The purpose of the fan was to control the convective heat transfer coefficient h to a steady value throughout the experiment. While blowing cool ambient air over a surface intended for heating may seem counterintuitive, without this forced convection boundary condition, intermittent gusts of wind and buoyant natural convection plumes would have introduced confounding and uncontrollable transient heat transfer processes into the experiment.

This experiment was situated at the approximate center of a 22.9 m by 5.49 m rectangular courtyard enclosed on all sides except for an 11.9 m wide walkway approaching from the south. The surrounding building was at least 5.5 m tall at all adjacent points, and it shielded the courtyard (and the experiment) from the wind. The experiments using unpainted, polished brass as the solar target were conducted on from 11:25 am to 1:47 pm (encompassing local noon) on March 11, 2008;

nine days before the Spring Equinox. The experiments using black-painted brass were conducted from 11:41 am to 1:32 pm (encompassing local noon) on September 15, 2008; seven days before the Autumnal Equinox. Both dates were selected because the sky was cloud-free and represented typical weather in Denton, Texas, USA. Testing dates near equinoxes were intentionally selected for these ambient-temperature-dependent solar experiments because these dates represent the average year-round ambient conditions. The choice to test between 11:00 am and 2:00 pm also mitigated large swings in ambient temperature and solar flux during the experiments because variations in these parameters during the three-hour time block are less severe than earlier or later in the day.

Both sets of experiments with unpainted brass and black-painted brass followed the same standard operating procedure. All logging instruments were started simultaneously with a sunlight blocker in place covering the Fresnel lens. The fan was set to run first at its "low" setting, and the experiment was allowed to thermally settle for at least ten minutes. At integer logging intervals, the sunlight blocker was removed to instantaneously expose the brass square to concentrated sunlight from the Fresnel lens. The brass square was heated and allowed to settle to a new steady state temperature. For these experiments, steady state was defined as an elevated temperature that did not fluctuate more than 7.0 K for 5 min. After the 5-minute steady state period was completed, the sunlight blocker was placed back on the Fresnel lens at an integer logging interval, and the brass square underwent Newtonian cool-down, eventually returning to ambient temperature. After 5 min, during which the brass square rested at ambient temperature, the fan velocity was increased to the next setting, "medium," and the process was repeated. The process was repeated once more with the fan set to "high." At the end of the experiment, all logged data were uploaded to a PC for processing and analysis.

Note in Figs. 9 and 10 the marked difference in energy reflectance between the unpainted (Fig. 9) and painted (Fig. 10) brass surfaces. This observation provides qualitative visual confirmation that adding black paint reduced the reflectance of the brass target in the second set of experiments.

F. Solar Collection Experiment at a 275.0:1.0 Concentration Ratio by Area

For these experiments, square pieces of Alloy 385 brass identical to the 28.8:1.0 concentrator experiment were prepared:5.46 ± 0.01 cm long by 5.46 ± 0.01 cm wide, and 0.33 ± 0.01 cm thick. As in the previous experiments, the brass surface was polished with 60-grit emery paper. In this set of experiments, one brass target was painted with three coats of Krylon BBQ and Stove paint, which left a dull black finish that could withstand temperatures up to 1200 °F (922 K). To measure the temperature of the target, a high-temperature Omega Engineering WTK-6-24-SMPW-M K-Type thermocouple was fixed to the brass target with an Alloy 385 brass #6 screw threaded into a hole machined at the center of the target. The screw and target materials were matched to minimize the anisotropic temperature gradients occurring at the

mismatching material interfaces. As shown in Fig. 11, sufficient slack was left on the thermocouple wire to allow for thermal expansion, and it was fed back to an Omega Engineering OM-2041 thermocouple reader mounted out of the sun. Temperature data were sampled at 1 Hz for the unpolished brass experiment and at 0.1 Hz for the black-painted brass experiment. Manufactured using "special limits or error" material, the thermocouple experimental error was $\pm$ 1.1 K, while the measurement error in the logger was ± 0.7 K for the temperature range of interest. Propagation of the experimental error yielded a measurement uncertainty no greater than $\pm$ 1.3 K.

As in the 28.8:1.0 area ratio experiment, the brass target was mounted within a close-fitting crevice etched into an insulating fireclay brick support with the thermocouple facing downward. The brick was held on a platform at the focus of a Fresnel lens such that as the lens moved to track the sun, the brick moved with it to remain at the focus (Fig. 11). The lens used for these experiments was a 104.1 ± 0.5 cm by 78.7 ± 0.5 cm rectangular Fresnel lens (area = 8192.7 ± 40.7 cm^2, 275 times the brass target area) mounted in a wooden frame above two bicycle wheels that allowed manual rotation of the lens in the elevation direction. These wheels were mounted on a large work surface that rotated manually on a lazy Susan 360° in the azimuthal direction (Fig. 12). The combination of motion in these two axes enabled 2-axis sun tracking.

The forced convection over the experiment was provided by a commercial off-the-shelf rotary fan with three qualitative settings: low, medium, and high. A conduit was fixed to the fan to concentrate its flow over brick and brass targets. The conduit included an internal honeycomb turbulence breaker to remove swirl and turbulent eddies from the airstream and promote laminar flow over the brass target.
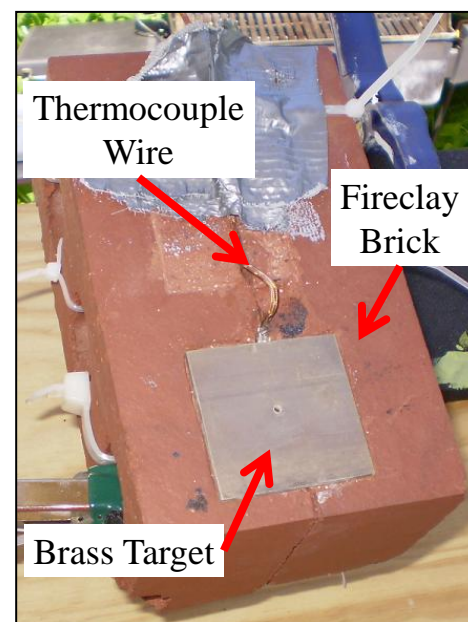

Fig. 11. *Ceramic mount that held the brass target in place under the large-area Fresnel concentrator. A K-type thermocouple bead was mechanically affixed to the bottom of the target, and its protruding wire was kinked to prevent thermal expansion from unseating the brass from the ceramic as the assembly warmed up.*
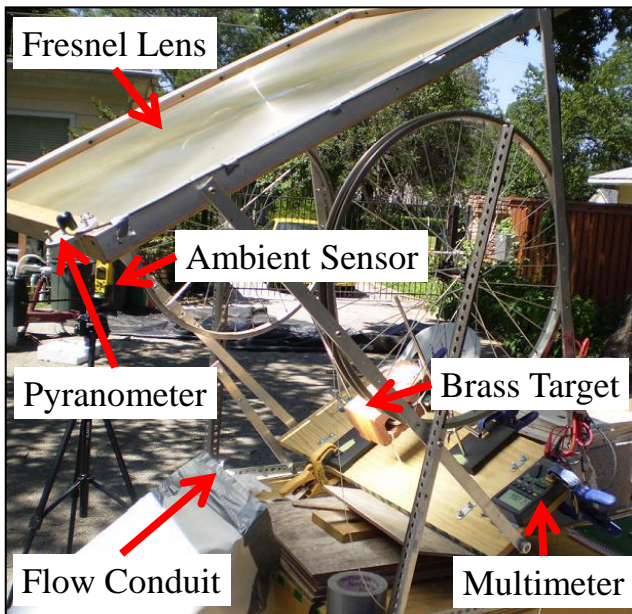
Fig. 12. *Large-Area Fresnel solar concentrator apparatus showing all the components used to regulate conditions and collect data.*

The air velocity, air temperature, and relative humidity over the brass square target and ceramic insulator were measured using a Kestrel 4500 pocket wind station mounted with an anemometer fan 12 ± 1 cm from the leading edge of the brick support and 9 ± 1 cm from the leading edge of the brass square. Data collected by this instrument were recorded at 0.0167 Hz, and the instrument's velocity, temperature, and relative humidity measurement uncertainties were ± 0.1 m/s, ± 1.0 K, and $\pm 3.0\%$ RH, respectively.

Unlike the 28.8:1.0 area ratio experiment, the ambient temperature and relative humidity for the 275:1.0 ratio experiment were measured by a stationary weather station located approximately 50 m from the experiment. A field calibrated Campbell Scientific HMP45C-L combined temperature and humidity probe enclosed within a 41303-5A RM solar radiation shield provided humidity with accuracy of $\pm 2\%$ RH and temperature with accuracy of ± 0.3 K at a sampling rate of 0.0167 Hz.

In addition, unlike the 28.8:1.0 area ratio experiment, which occurred in an enclosed courtyard, the 275:1.0 area ratio experiment was performed in an open field, which allowed longer experimental sessions, as the sun was not obscured by buildings in the morning or afternoon. To shield the experiment from wind gusts, a canvas shroud was stapled all the way around the wooden frame holding the Fresnel lens and allowed to hang down past the brick-and-brass target. While the shroud allowed all focused sunlight incident on the Fresnel lens to enter the experiment, evaluation of the shrouded volume with a hot wire anemometer showed that the wind gusts were blocked from disturbing the air over the brass target.

Experiments with a 275:1.0 area ratio were conducted on two cloud-free days: May 16 and 17, 2009. To measure instantaneous solar flux, an Apogee SP-110 pyranometer was mounted on the Fresnel lens frame in the same plane as the lens

(Fig. 12). This arrangement ensured that the pyranometer and lens aperture always maintained angles identical to those of the Sun. The pyranometer was connected to an Extech MultiMaster® 570 true RMS logging multimeter, and the combined uncertainty in the solar flux measurement was ± 10 W/m^2. A pyranometer multimeter logged the data at 1 Hz.

Both sets of 275:1.0 area ratio experiments with unpainted brass and black painted brass followed the same standard operating procedure for the 28.8:1.0 area ratio experiments described above.

VI. RESULTS

A. 28.8:1.0 Area Ratio Experiment

The time–temperature histories for both the unpainted and painted brass targets with a 28.8:1.0 area ratio for sunlight concentration are shown in Figs. 13 and 14, respectively. The charts are plotted with the same ordinate scaling to accentuate the peak temperature difference caused by the lack or presence of the black paint surface coating. The peak temperatures achieved for each fan setting and surface treatment are shown in Fig. 13 and Table 2.

Table 2 summarizes other quantitative results from this series of experiments. For all six conditions, the forced convective and irradiative heat transfer coefficients over the brass target, h, were calculated by fitting the Newtonian cool-down curve of (9) to the experimental data, with h as a variable fitting parameter. The standard error of the estimate (SEE) between (9) and the experimental data was calculated for the complete cool-down period in each of the six tests, and the closest integer value of h was selected to minimize the SEE for each experiment.
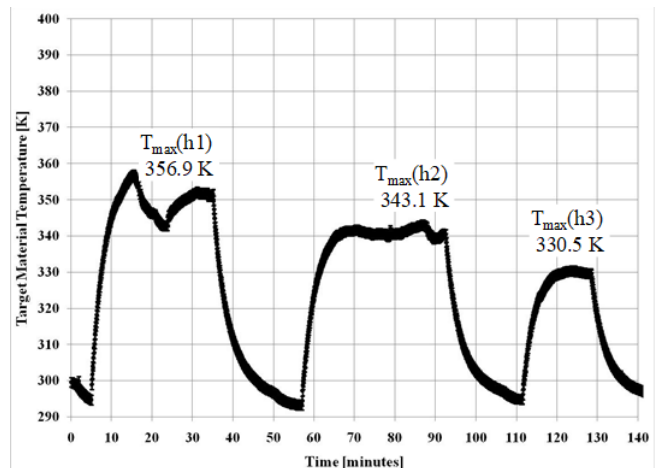

Fig. 13. *Temperature-time histories for the unpainted brass target under concentrated sunlight at three different qualitative fan velocity settings: low, medium, and high with a 28.8:1.0 concentrator-to-target area ratio. Experimental uncertainty in these data coincides with data point size.*

The forced convection coefficient is expected to increase with increasing velocity over the brass piece, which is the case in this set of experiments. From the calculated h and the experimentally measured maximum brass target and average ambient temperatures, (8) was solved for the steady-state power absorbed by the brass target. The peak temperature was then

used in (1) with $T_{TE,cold} = 300$ K to estimate the efficiency of the heat-to-electrical energy conversion and the power output that might be expected if a TEG was in place. Finally, the energy incident on the brass target was compared with the energy absorbed to calculate the percentage of the reflected energy. For the 28.8:1.0 area ratio experiments, a pyranometer was not available to directly measure the instantaneous solar flux, and an estimate of 1000 W/m^2 was assumed. As explained above, the local peak solar flux shown in Fig. 4 confirms the validity of this assumed flux value.
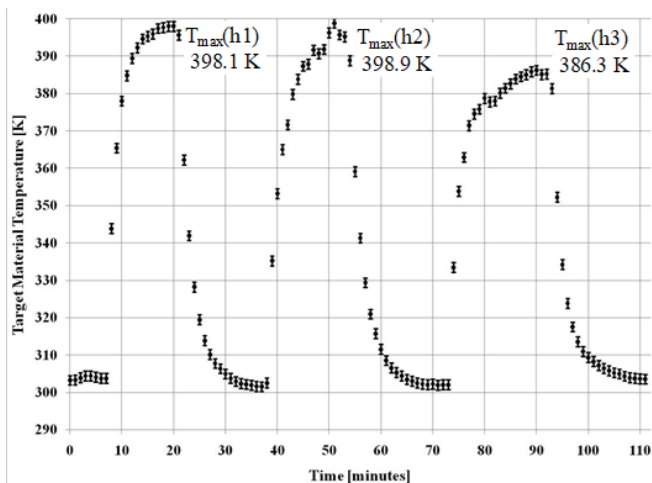

Fig. 14. *Temperature-time histories for black painted brass target under concentrated sunlight at three different qualitative fan velocity settings: low, medium, and high with a 28.8:1.0 concentrator-to-target area ratio.*

TABLE II
MEASURED AND CALCULATED EXPERIMENTAL PARAMETERS OF BRASS TARGET UNDER CONCENTRATED LIGHT:
28.8:1.0 CONCENTRATOR AREA RATIO

Unpainted Brass			
Max. Temp [K]	356.9	343.1	330.0
Fan Setting [-]	Low	Medium	High
Ave. Vel [m/s]	0.72±0.18	1.27±0.23	1.35±0.20
h [W/m^2-K]	38	40	48
Power Absorbed [W]	6.6	5.7	4.8
Generation Potential [W]	0.10	0.07	0.04
ρ ($\dot{E}_{sun}$=1000 W/m^2) [%]	92	93	94
Painted Brass			
Max. Temp [K]	398.1	398.9	386.3
Fan Setting [-]	Low	Medium	High
Ave. Vel [m/s]	2.56±0.57	3.15±1.08	3.63±1.12
h [W/m^2-K]	68	63	71
Power Absorbed [W]	19.4	17.6	17.4
Generation Potential [W]	0.50	0.46	0.40
ρ ($\dot{E}_{sun}$=1000 W/m^2) [%]	77	80	80

B. 275.0:1.0 Area Ratio Experiment

The time–temperature histories for unpainted and painted brass targets with 275.1:1.0 area ratio are given in Figs. 15 and 16, respectively. These charts are plotted with the same ordinate scaling to accentuate the peak temperature difference caused by

lack or presence of black paint surface coating. The peak temperatures achieved for each fan setting and surface treatment are shown in Figs. 15 and 16 and Table 3; this table also summarizes other quantitative results from this series of experiments.

The same calculation and evaluation processes used for the 28.8:1.0 area ratio data were used to evaluate the performance of the larger Fresnel lens, giving calculated values for h, steady-state power absorption, estimated efficiency, and estimated TEG energy output. Finally, the energy incident on the brass target was compared with the energy absorbed to calculate the percentage of the reflected energy. A pyranometer was used to directly measure the instantaneous solar flux. The solar reflectivity was then evaluated for both surface treatments (i.e., polishing versus black paint) by comparing the average solar flux in the steady-state period to the rate of energy absorption.

C. PV Efficiency Degradation at Elevated Temperature

Fig. 17 combines all the modeling and experimental data described to this point into a single culminating graphic for PV and TEG. (1) for TEG is presented in green, and (2) for PV is given in yellow. Representing performance parameters for their respective solid state energy converters these curves cross at 495 K. This is maximum possible temperature at which TEG efficiency exceeds PV efficiency under identical conditions.
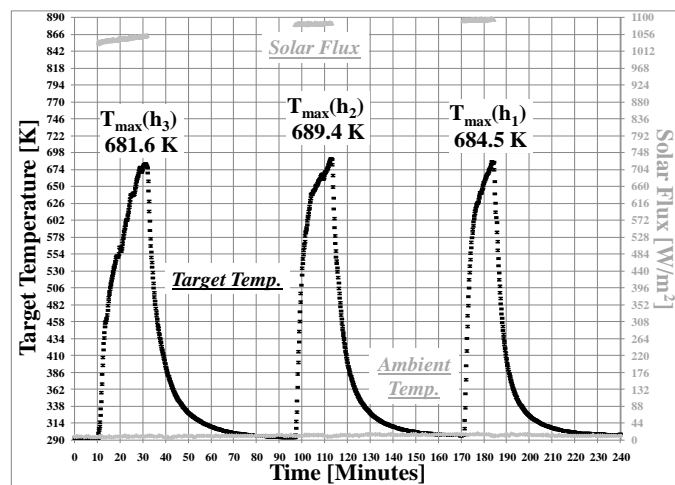

Fig. 15. *Temperature-time histories of the 275.0:1.0 area ratio experiments for an unpainted brass target at three different qualitative fan velocity settings: "low", "medium", and "high". Pyranometer solar flux data, recorded during each warm-up/cool-down event is shown in the second Y axis. Experimental uncertainty in these data coincides with data point size.*

The experimental PV output degradation with temperature is shown in Fig. 17 using red (for heat-up) and blue (for cool-down) data points. Extrapolating these data to 300 K (purple curve) indicates the PV room temperature efficiency is 3.7%, instead of 12% reported in the literature. Both a Root Mean Square Error (RMSE) analysis and an R^2 analysis were conducted to aggregate the magnitudes of the errors between the model and experimental data into single measures of the model's predictive power. Both the PV warmup and cooldown data were included in these analyses to capture the effects, if any, on the heating direction hysteresis impacts on the

predictive linear model. The resulting RMSE value was 0.000329 with a Normalized RMSE of 0.418. The resulting R^2 value was 0.994, and its close agreement with unity indicates the model's exceptional PV efficiency predictive ability over the studied temperature range.
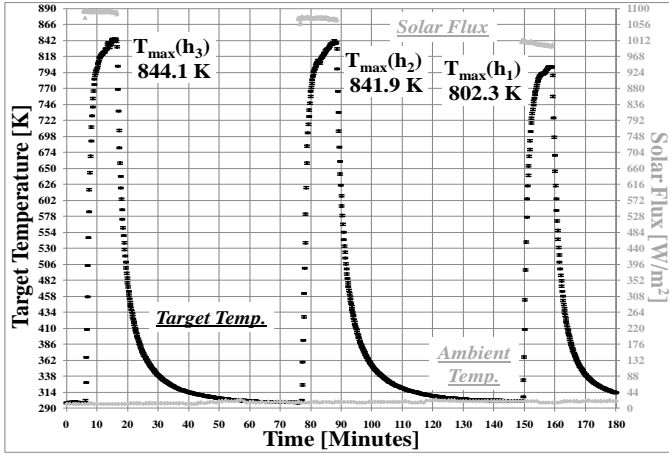

Fig. 16. *Temperature-time histories of the 275.0:1.0 area ratio experiment for a brass target coated in refractory black paint at three different qualitative fan velocity settings: "low", "medium", and "high". Reduced reflectivity owing to the paint coating yields increased energy absorption, which manifests as increased peak steady state target temperature compared to the data sets with unpainted targets. Pyranometer solar flux data, recorded during each warm-up/cool-down event is shown in the second Y axis. Experimental uncertainty in these data coincides with data point size.*

TABLE III
MEASURED AND CALCULATED EXPERIMENTAL PARAMETERS OF BRASS TARGET UNDER CONCENTRATED LIGHT:
275.0:1.0 CONCENTRATOR AREA RATIO

Unpainted Brass			
Max. Temp [K]	681.6±1.3	689.4±1.3	684.5±1.3
Fan Setting [-]	Low	Medium	High
Ave. Vel [m/s]	0.53±0.40	0.75±0.25	1.05±0.56
h [W/m²-K]	27	30	36
Power Absorbed [W]	30.9	34.8	41.3
TEG Efficiency [-]	0.091	0.093	0.092
Generation Potential [W]	2.815	3.227	3.787
ρ ($\dot{E}_{sun}$=1000 W/m²) [%]	96	96	95
Painted Brass			
Max. Temp [K]	844.1±1.3	841.9±1.3	802.3±1.3
Fan Setting []	Low	Medium	High
Ave. Vel [m/s]	0.98±0.40	1.03±0.28	0.94±0.10
h [W/m²-K]	42	42	47
Power Absorbed [W]	68.2	67.5	70.3
TEG Efficiency [-]	0.123	0.123	0.115
Generation Potential [W]	8.407	8.292	8.106
ρ ($\dot{E}_{sun}$=1000 W/m²) [%]	92	92	91

The intersection between these data and the TEG model suggests that TEG becomes more efficient than PV above 375 K. Finally, the blue curve represents the PV model in (2), but with 3.7% efficiency at 300 K. The TEG curve efficiency

crossover temperature for the PV model was 400 K. These later crossover points represent more realistic temperatures based on experimental measurements where the TEG efficiency exceeds the PV efficiency.
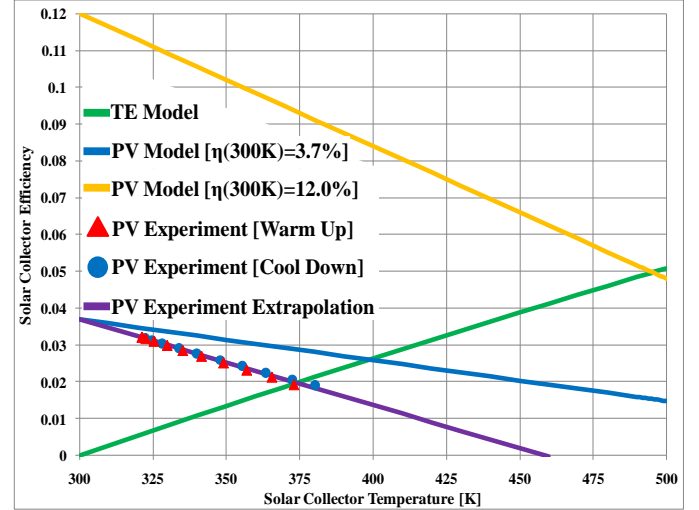

Fig. 17. *Experimental data and efficiency model curves for a variety of PV and TEGs. Uncertainty in the PV experiment data coincides with data point size.*

VII. DISCUSSION

A. PV Performance Under Concentrated Sunlight

Fig. 17 shows the experimentally measured linear efficiency degradation of a real PV with respect to temperature, in excellent quantitative agreement with the prevailing simple linear model for this system of (2). A linear extrapolation of these performance data (2) indicates a probable efficiency crossover temperature for TEG and PV CSP systems of approximately 375 K (compared to 495 K originally calculated from the upper-bound PV model). The 375 K crossover temperature is within the range of the 28.8:1.0 area ratio concentrator and lens target treated with black paint (Fig. 14 and Table 2). This experimental result demonstrates that the assumptions made to model the PV performance in (2) are optimistic and likely represent an upper bound on the performance with respect to a real system.

Although not considered analytically, PV efficiency degradation with increased solar flux intensity was shown to occur experimentally from the results of Fig. 8 with diminishing returns at 1600 W/m² solar flux and complete saturation at 2000 W/m². This saturation effect severely reduces CSP PV efficiency. The typical (un-concentrated) peak solar flux is 1000 W/m², and these results indicate that no additional power output increase could be realized under peak flux for concentrator aperture-to-PV cell area ratios larger than 2. In contrast, increased TEG efficiency was verified to occur at least up to 471 K for Bi_2Te_3 [30], which corresponds to a concentrator area ratio of at least 200 [using (4)]. Thus, the economic benefit of increasing A_{lens}/A_{target} for a given solid-state generator is dramatically more pronounced for TEG than for PV.

B. TEG Performance Under Concentrated Sunlight

A general result for the TEG hot-side lens experiment under CSP is that a higher forced convection over the target decreases the maximum achievable temperature while also decreasing the absorbed power. This experimental result is also apparent in the theoretical model based on the temperature and thermal energy absorption coupling in (8). Because a high rate of thermal energy absorption is important for maximizing TEG energy generation, careful design of the TEG hot-side absorber is required to mitigate unwanted heat loss from forced convection (wind gusts) and buoyant natural convection. However, simultaneously increasing the TEG hot-side temperature and absorbed heat might prove to be dilatory. It has been assumed in the bounding analyses presented here that the thermoelectric figure of merit, z, remains fixed as the temperature increases. In reality, z degrades with elevated temperature. The experimental results of Muto et al. [27] indicated that the benefits of increasing the temperature for the device figure of merit (zT) are nearly exhausted at 471 K for Bi_2Te_3. This temperature was exceeded in the 275.0:1.0 area ratio experiments with both unpainted and black-painted targets (Fig. 15, and 16, and Table III).

While TEG materials designed for high efficiency at elevated temperatures provide a path to capitalize on high heat absorption and high temperatures, an alternative approach that is compatible with existing well-characterized TEG materials is to design for high heat absorption while passively regulating the TEG material temperature to within an optimal range. The question of whether active or passive CSP TEG cooling is most effective was explored by Alamri et al., who concluded that the passive approach is superior for individual TEG generators of centimeters in characteristic size [21].

When considering TEG cooling, heat lost from the hot side by convection and radiation cannot be converted to electricity and should be minimized, and the heat conducted through the TEG material undergoes beneficial conversion to electricity. Connecting a heat sink to the deep ground (as shown in Fig. 1) to pull heat at a high rate through the TEG would maintain a reasonable operating temperature.

C. Economic Analysis of PV vs. TEG for CSP

While a detailed economic analysis is not the goal of this study, a simple payback analysis demonstrates the additional cost-benefit of deploying TEG over PV in CSP applications without cooling. An example cost analysis by Tomosk et al. [41] provides a foundation. The study was conducted for Las Vegas, NV, USA, near the Amargosa Valley project described in the opening paragraph of this paper. A 100 kW_{peak} CSP PV installation without cooling was analyzed, and it was estimated to produce 192,493 kWh/year of electricity. For installation in 2016 and 25 years of projected operation, the resulting Levelized Cost Of Electricity (LCOE) was $0.0980/kWh for this system. Compared to $0.12150/kWh, the average commercial electricity rate in Las Vegas [42], the analyzed system generates $0.0235/kWh or $4523.58/yr in net financial returns. Using the middle capital cost scenario given by Tomosk et al. for the 2016 CSP installation gives a total

installed cost of $180,000 with a resulting simple payback period of 39.8 years. Tomosk et al. commented that this CSP PV installation is a money-losing proposition for a 25-year projected system operational life.

Owing to their manufacturing process and lack of current major energy generation applications, TEGs are not available in large peak watt configurations of 320 W_{peak} and above, such as PV used in CSP systems. Therefore, a fair and representative TEG/PV cost comparison was made by comparing 60 W_{peak} PV ($85.99/panel) with commercially available 60 W_{peak} TEG ($8.99/panel). For the 100 kW_{peak} CSP system analyzed, 1667–60 W_{peak} panels of either PV or TEG are needed. This cost is $143,345 for PV, meaning the balance of plant installation cost is $180,000–$143,345 = $36,655. Assuming the optics and balance of the plant for a CSP TEG system cost the same as a PV installation, the cost to install a 100 kW_{peak} CSP TEG plant is $36,655 + $14,986 = $51,641.

This study showed that the PV efficiency is inferior to the TEG efficiency under CSP conditions. Nonetheless, if their efficiencies are assumed to be the same, the simple payback period for the CSP TEG in this scenario would be 11.42 years. The upfront CSP TEG installation cost is less than CSP PV for a similarly sized system because the panels are much cheaper. Moreover, the resulting simple payback period is more than 28 years shorter! In addition, the economics of the modeled CSP TEG plant make it a profitable venture, whereas a CSP PV plant with equivalent generating capacity would fail financially.

D. Target Surface Reflectance

Experimental thermal performance of brass TEG surrogate hot-end collector targets with and without black paint treatment revealed that the energy reflectance from the collector target surface under concentrated sunlight severely limits the rate of thermal power absorption. Moreover, the reflectance values obtained from the measured parameters disagreed with the values reported in the literature. White light reflectance of emery-paper-polished brass was reported to be 73.8% [36], while these experiments revealed 92% to 96%. Black surface coating was expected to reduce reflectivity to 6% [37], but the measured ρ was only 77 to 80% for acrylic-based black paint and 91 to 92% for refractory black paint.

These discrepancies cannot be attributed to energy re-radiation from the target because 1) the targets were not observed to glow with self-incandesce, and 2) cool-down curves were used to estimate the convective and radiative heat transfer coefficients, h. This approach automatically lumped radiation into the calculation of h. The radiation's impact, therefore, is present in the model of (8) and (9) and is attributed to the fact that the observed reflectivity discrepancies would be double counting.

Instead, we hypothesize that the observed disparity results from a combination of the two factors. First, the cited literature values are for sunlight incident normal to a surface, whereas the Fresnel lens of our experiments focused sunlight at the target surface at a range of off-normal angles, which may have promoted reflection. Second, black paint selection was not

based on high solar absorptivity, but rather on survivability at high temperatures. Thus, while the surface coatings might have appeared black to the naked eye, their actual reflectivity was likely much higher than that of the coatings specifically designed to absorb sunlight. This supposition is especially pronounced for refractory paint, whose purpose is to mark, coat, and protect surfaces from high temperatures [38] by reflecting heat from those surfaces.

E. Surface Treatment Temperature Survivability and Selection Options

While acrylic-based paint provided superior low-reflectivity performance between the two tested paints, it burned off above 400 K and could not be reliably used for the 275.0:1.0 area ratio tests, which all reached above 680 K. While the refractory paint survived even at the highest experimental temperatures recorded, it only marginally reduced the reflectivity below the value measured with no surface coating. Fig. 18 shows a qualitative survivability comparison between the acrylic and refractory paints on brass targets after exposure to temperatures exceeding 680 K in the 275.0:1.0 area ratio experiment.
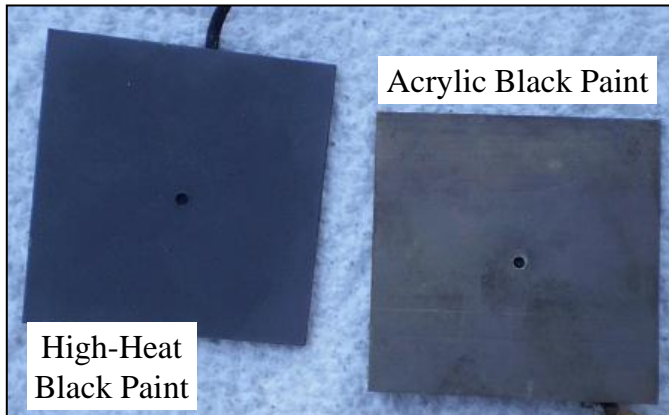

Fig. 18. High solar flux exposure burned off acrylic-based paint (right), while BBQ & Stove paint (left) survived. Surface treatments with low reflectivity that can withstand high heat are needed to improve efficiency.

The experiments performed show that the most severely limiting CSP TEG system efficiency is the surface reflectivity to incident concentrated sunlight (even after surface treatment). The identification of low-reflectivity surface coatings that can withstand high heat and concentrated sunlight is a possible solution. Unlike PV cells, which can only utilize surface coatings that allow light to pass through the PV material for absorption, TEG coatings do not need to be transparent. The coating itself can absorb the incident energy and transmit it by conduction to the TEG hot side. Thus, the choice of possible TEG hot-side lens surface coatings is broader than that of the PV coatings, and the opportunity to reduce reflectivity is greater.

For an example, a manmade material with the best all-color sunlight transmission properties has an integrated total reflectance of 3.79% [39], while a material with the best total optical absorption properties has an integrated total reflectance of 0.045% [40]. Instead of focusing on surface coatings, another design option is to encapsulate the TEG hot side target within an insulated cavity that allows concentrated sunlight to easily enter, but makes it difficult to escape.

F. Analysis of Theoretical Modeling Versus Experiments for 28.2:1.0 Area Ratio

The experimental solar lens area to TEG hot side target area ratios were selected from (4) (which included heat conduction from the TEG) and (5) (which did not consider heat conduction from the TEG). The goal of (4) and (5) was to estimate lens A_{lens}/A_{target} ratios to achieve the theoretical maximum PV versus TEG efficiency crossover temperature of $T_{TE,hot} = 495$ K for polished, unpainted brass based on estimated values of k, L, T_∞ and especially $\dot{E}_{sun}$, h, and ρ prior to experimental measurement of these parameters.

Because it did not consider conduction in the TEG, (5) was the most representative of the expected thermal performance of the TEG hot side target alone, and it guided the selection of the 28.8:1.0 area ratio experiment design for unpainted brass targets. For the 28.8:1.0 area ratio, the peak (unpainted) target temperature achieved was 356.9 ± 1.3 K (almost 140 K lower than predicted). However, the predicted h was 21.7 W/m^2-K while actual values ranged from 38 to 48 W/m^2-K. The expected ρ was 73.8%, while the actual values ranged from 95 to 96%.

Given the measured values for these parameters from the tests reported here and experimental guidance, the efficiency crossover temperature threshold for PV and TEG is likely approximately 375 K rather than 495 K. (5) suggests an area ratio of approximately 31 to 45 to achieve efficiency crossover when the TEG hot-side target material is treated with a refractory black coating.

G. CSP Design Recommendations Arising from 275.0:1.0 Area Ratio Experiments

(4) includes the heat conduction through the TEG material and is the most representative of the proposed energy-generating configuration shown in Fig. 1. Using the parameters experimentally determined from the tests reported here, (4) suggests an area ratio of approximately 317 to 357 to achieve TEG and PV efficiency crossover when the TEG target material is treated with a refractory black coating. If other design drivers indicate area ratios below these threshold values, PV remains the CSP solid-state energy converter of choice, provided that the threshold for PV efficiency saturation at elevated solar flux intensity is not exceeded for the PV cells used.

However, if a real CSP PV power generation application (where cooling is unavailable) has an A_{lens}/A_{target} that exceeds ~350, TEG must be considered as an alternative to PV. Moreover, with improved surface coatings designed to absorb both concentrated sunlight and survive high CSP operating temperatures, the A_{lens}/A_{target} ratio at which the TEG should be considered instead of the PV drops.

VIII. CONCLUSION

It was argued that there exists a practical operating regime in which TEG is superior to PV for CSP, such as for terrestrial sites without co-generation and no liquid water for cooling.

Based on modeling assumptions, the upper and lower bounds were applied to PV and TEG performance, respectively. These bounding assumptions were verified experimentally for PV and the empirical literature results for TEG.

The performances of the models were then compared to identify the temperature at which TEG efficiency exceeds that of the PV, which was approximately 495 K. The efficiency crossover temperature of a real PV is likely closer to 375 K, based on an experimental investigation of real PV performance under elevated temperatures and photon flux consistent with concentrated sunlight.

As a result of a thermal performance model that predicted the lens-aperture-to-TEG-target area ratios at this crossover, two experimental apparatuses were designed: one with an area ratio of 28.8:1.0, and the other with an area ratio of 275.0:1.0. A brass square 5.46 cm long and 0.33 cm thick was used as the TEG generator hot side target and placed at the lens focus to collect solar energy. TEGs were not used in these tests. The target was subsequently treated with black paint to improve its thermal performance.

We showed experimentally that the TEG hot-side target can easily be heated beyond the TEG/PV efficiency crossover temperature using concentrated sunlight (maximum temperature = 398.9 ± 1.3 K for the 28.8:1.0 area ratio experiment and 844.1 ± 1.3 K for the 275.0:1.0 area ratio experiment). As a caveat, these tests did not consider the impact of the heat conducted through the TEG on the hot side target temperature. Nonetheless, given the high thermal resistivity of TEG materials, the expected results will be similar when considered. This question will be explored in future work.

Using the experimentally measured parameters in a predictive model, a sunlight concentration ratio of 317 to 357 was estimated to sufficiently achieve the efficiency crossover temperature when the TEG material was used for energy generation. Had a TEG been in place during the experiments described here, the power generation potential under the smaller Fresnel lens (28.8:1.0 area ratio) would have been 0.4 to 0.5 watts while the potential under the large lens (275.0:1.0 area ratio) would have been 8.1 to 8.4 watts. Thus, this technique shows promise for future investigations with TEG energy converters in place for power production. Moreover, it suggests that for real CSP PV power generation applications where cooling is not available and where A_{lens}/A_{target} exceeds ~350, TEG is considered as an alternative to PV.

A significant future challenge for making TEG competitive with PV for CSP is the development of surface coatings with high solar absorptivity that can survive high temperature. The surface reflectivity under concentrated solar flux must be dramatically reduced below the reflectivities of the coatings used in the current experiments to make TEG a viable PV alternative in CSP. One coating used in these experiments burned off above 400 K, whereas the second coating reduced reflectivity only marginally from 91% to 95% compared to unpainted, polished brass. Given high target solar reflectivity of the coatings used, at most no more than 23% of the available incident energy was collected in the 28.8:1.0 area ratio experiment, and no more than 9% was collected in the 275.0:1.0

area ratio experiment. Now that the TEG hot side target thermal performance is understood and characterized, the implementation of a functioning experimental CSP TEG system designed for remote, coolant-free power generation will be pursued in future work.

IX. REFERENCES

[1] HELIOSCSP Solar Thermal Energy News, "HeliosCSP Solar Thermal Energy News," 02 February 2020. [Online]. Available: https://helioscsp.com/concentrated-solar-power-had-a-global-total-installed-capacity-of-6451-mw-in-2019/. [Accessed 20 January 2023].

[2] H. A. Radwan, M. A. Sayed, T. Takeshita, A. A. Elbaset and G. Shabib, "High-Frequency Isolated Three-phase Grid-Tied PV Converter Based a New Boost Inverter Topology," *International Journal of Applied Energy Systems,* vol. 4, no. 2, pp. 33-39, 2022.

[3] R. B. Laughlin, "Amargosa Desert: Worthless Habitat?," 14 May 2009. [Online]. Available: http://large.stanford.edu/publications/power/references/amargosa/.

[4] Sunshine Valley O&M Office, "EDP Renewables North America," 2021. [Online]. Available: https://www.edpr.com/north-america/sites/edprna/files/2021-10/NV%20Sunshine%20Valley%20Fact%20Sheet%202021.pdf. [Accessed 09 September 2022].

[5] D. Narducci and B. Lorenzi, "Hybrid thermoelectric-photovoltaic solar harvesters: technological and economic issues," *Japanese Journal of Applied Physics,* vol. 62, no. SD, 2022.

[6] Mustofa, Z. Djafar, Syafaruddin and W. H. Piarah, "A new hybrid of photovoltaic-thermoelectric generator with hot mirror as spectrum splitter," *Journal Of Physical Sciences,* vol. 29, no. 2, pp. 63-75, 2018.

[7] L. Ma, Q. Zhao and H. Zhang, "Performance analysis of a new hybrid system composed of a concentrated photovoltaic cell and a two-stage thermoelectric generator," *Sustainable Energy, Grids and Networks,* vol. 27, 2021.

[8] A. Lashin, M. Al Turkestani and M. Sabry, "Concentrated Photovoltaic/Thermal Hybrid System Coupled with a Thermoelectric Generator," *Energies,* vol. 12, no. 13, p. 2623, 2019.

[9] I. Manderekal, M. C. Halford and R. Boehm, "Simulation and Optimization of a Concentrated Photovoltaic System," *J. Sol. Energy Eng.,* vol. 128, no. 2, pp. 139-145, May 2006.

[10] A. Rabl and R. Winston, "Ideal concentrators for finite sources and restricted exit angles," *Applied Optics,* vol. 15, no. 11, pp. 2880-2883, 1976.

[11] E. M. Kritchman, A. A. Friesem and G. Yekuteli, "Highly concentrating Fresnel lenses," *Applied Optics,* vol. 18, no. 15, pp. 2688-2695, 1979.

[12] A. Hande, T. Polk, W. Walker and D. Bhatia, "Indoor solar energy harvesting for sensor network router nodes," *Microprocessors and Microsystems,* vol. 31, no. 6, pp. 420-432, 2007.

[13] C. Fallwell, D. Davis and M. Traum, "Assessing Energy Conversion Efficiency for Sub-Kilowatt Thermoelectric Generators Under Concentrated Sunlight," in *AIAA*, Denton, TX, 2008.

[14] D. Rowe, CRC handbook of thermoelectrics, Boca Raton: CRC Press, 1995.

[15] H. Xi, L. Luo and G. Fraisse, "Development and applications of solar-based thermoelectric technologies," *Renewable and Sustainable Energy Reviews,* vol. 11, no. 5, pp. 923-936, 2007.

[16] N. Q. Nguyen and K. V. Pochiraju, "Behavior of thermoelectric generators exposed to transient heat sources," *Applied Thermal Engineering,* vol. 51, no. 1-2, pp. 1-9, 2013.

[17] S. Maneewan, J. Khedari, B. Zeghmati, J. Hirunlabh and J. Eakburanawat, "Investigation on generated power of thermoelectric roof solar lens," *Renewable Energy,* vol. 29, no. 5, pp. 743-752, 2004.

[18] G. Boyle, Renewable Energy: Power for a Sustainable Future, 2nd ed., Oxford: Oxford University Press, 2004.

[19] D. Kraemer , L. Hu, A. Muto, X. Chen, G. Chen and M. Chiesa, "Photovoltaic-thermoelectric hybrid systems: A general optimization methodology," *Applied Physics Letters,* vol. 92, no. 24, 2008.

[20] Y. Vorobiev, J. Gonzalez-Hernandez, P. Vorobiev and L. Bulat, "Thermal-photovoltaic solar hybrid system for efficient solar energy conversion," *Solar Energy,* vol. 80, no. 2, pp. 170-176, 2006.

[21] S. Alarmi, T. Alarmi, M. Akbar, F. Hadi and M. Traum, "Evaluating Forced Versus Natural Convection for Solar Concentrating Hybrid Photovoltaic-Thermoelectric Power Systems Made from Small Up-Cycled Satellite Dishes," in *ASME 2017 International Mechanical Engineering Congress and Exposition (IMECE2017)*, Tampa, Florida, 2017.

[22] S. B. Riffat and X. Ma, "Thermoelectrics: a review of present and potential applications,," *Applied Thermal Engineering,* vol. 23, no. 8, pp. 913-935, 2003.

[23] G. Rockendorf, R. Sillmann, L. Podlowski and B. Lizenburger, "PV-Hybrid and Thermoelectric Lenss," *Solar Energy,* vol. 67, no. 4-6, pp. 227-237, 1999.

[24] H. Naito, Y. Kohsaka, D. Cooke and H. Arashi, "Development of a solar receiver for a high-efficiency thermionic/thermoelectric conversion system," *Solar Energy,* vol. 58, no. 4-6, pp. 191-195, 1996.

[25] A. O. Ochieng, T. F. Megahed, S. Ookawara, Hassan and H. Hassan, "Comprehensive Review in Waste Heat Recovery in Different Thermal Energy-Consuming Processes Using Thermoelectric Generators for Electrical Power Generation," *Process Safety and Environmental Protection,* vol. 162, pp. 134-154, 2022.

[26] G. Min, D. M. Rowe and K. Kontostavlakis, "Thermoelectric figure-of-merit under large temperature differences," *Applied Energy,* vol. 123, pp. 1301-1304, 2014.

[27] A. Muto, D. Kraemer, Q. Hao, Z. F. Ren and G. Chen, "Thermoelectric properties and efficiency measurements under large temperature differences," *Review of Scientific Instruments,* vol. 80, no. 9, pp. 3901-3908, 2009.

[28] A. Lashin, M. Al Turkestani and M. Sabry, "Performance of a Thermoelectric Generator Partially Illuminated with Highly Concentrated Light," *Energies,* vol. 13, no. 14, p. 3627, 2020.

[29] D. M. Rowe, CRC Handbook of Thermoelectric, 1st ed., Boca Raton, FL: CRC Press, 1995.

[30] R. Robert, L. Bocher, B. Sipos, M. Döbeli and A. Weidenkaff, "Ni-doped cobaltates as potential materials for high temperature solar thermoelectric converters," *Progress in Solid-State Chemistry,* vol. 35, no. 2-4, pp. 447-455, 2007.

[31] H. Scherrera, L. Vikhorb, B. Lenoira, A. Dauschera and P. Poinasc, "Solar thermoelectric generator based on skutterudites," *Journal of Power Sources,* vol. 115, no. 1, pp. 141-148, 2003.

[32] J. Tester, E. M. Drake, M. J. Driscoll, M. W. Golay and W. A. Peters, in *Sustainable Energy Choosing Among Options*, Cambridge, MA, The MIT Press, 2005, p. 576.

[33] H. Shen, H. Lee and S. Han, "Optimization and fabrication of a planar thermoelectric generator for a high-performance solar thermoelectric generator," *Current Applied Physics,* vol. 22, pp. 6-13, 2021.

[34] E. Skoplaki and J. A. Palyvos, "On the temperature dependence of photovoltaic module electrical performance: A review of efficiency/power correlations," *Solar Energy,* vol. 83, no. 5, pp. 614-624, 2009.

[35] G. Notton, C. Cristofari, M. Mattei and P. Poggi, "Modeling of a double-glass photovoltaic module using finite differences," *Applied Thermal Engineering,* vol. 25, no. 17-18, pp. 2854-2877, 2005.

[36] Y. Kemmoku, T. Egami, M. Hiramatsu, Y. Miyazaki, K. Araki, N. J. Ekins-Daukes and T. Sakakibara, "Modeling of Module Temperature of a Concentrator PV System," in *19th European Photovoltaic Solar Conference and Exhibition*, Paris, France, 2004.

[37] P. Wang, J. E. Li, B. L. Wang, T. Shimada, H. Hirakata and C. Zhang, "Lifetime Prediction of Thermoelectric Devices under Thermal Cycling," *Journal of Power Sources,* vol. 437, 2019.

[38] A. Annino, F. Grasso, F. Musumeci and A. Triglia, "Spectral Absorptivity of Rough Copper and Brass Surfaces," *Applied Physics A: Solids and Surfaces,* vol. 35, pp. 115-118, 1984.

[39] A. F. Mills, Basic Heat and Mass Transfer, Pearson College Div, 1999.

[40] Y. Cengel, A. J. Ghajar and J. Hajar, Heat and Mass Transfer: Fundamentals and Applications, New York, NY: McGraw-Hill, 2011.

[41] S. Tomosk, D. Wright, K. Hinzer and J. E. Haysom, "Analysis of Present and Future Financial Viability of High-Concentrating Photovoltaic Projects," in *High Concentrator Photovoltaics*, Switzerland, Springer, Cham, 2005, pp. 377-400.

[42] Electricity Local, "Las Vegas Electricity Rates," Electricity Local, [Online]. Available: https://www.electricitylocal.com/states/nevada/las-vegas. [Accessed 19 January 2023].

[43] C. Fallwell, D. Davis and M. Traum, "Solar Energy Concentration for Thermoelectric Power Generation at the Sub-Dekawatt Scale," in *41th AIAA Thermophysics Conference*, San Antonio, Texas, 2009.

[44] B. Lorenzi and G. Chen, "Theoretical Efficiency of Hybrid Solar Thermoelectric-Photovoltaic Generators.," *Journal of Applied Physics,* vol. 124, no. 2, 2018.

[45] V. Quasching, in *Understanding Renewable Energy Systems*, London, UK, Earthscan Publicationa, Ltd., 2005, p. 138.

[46] A. Lekbir, M. Meddad, A. Eddiai, S. Benhadouga and R. Khenfer, "Higher-efficiency for combined photovoltaic-thermoelectric solar power generation," *International Journal of Green Energy,* vol. 16, no. 5, pp. 371-377, 2019.